


# Quantum phases and the spectrum of collective modes in a spin-1 Bose-Einstein condensate with spin-orbital-angular-momentum coupling

Paramjeet Banger<sup>1,\*</sup>, Rajat<sup>1,†</sup>, Arko Roy<sup>2,‡</sup> and Sandeep Gautam<sup>1,§</sup>

<sup>1</sup>*Department of Physics, Indian Institute of Technology Ropar, Rupnagar-140001, Punjab, India*

<sup>2</sup>*School of Physical Sciences, Indian Institute of Technology Mandi, Mandi-175075 (H.P.), India*

 (Received 5 July 2023; revised 31 August 2023; accepted 11 October 2023; published 25 October 2023)

Motivated by recent experiments [Chen *et al.*, *Phys. Rev. Lett.* **121**, 113204 (2018); Chen *et al.*, *ibid.* **121**, 250401 (2018)], we investigate the low-lying excitation spectrum of the ground-state phases of spin-orbital-angular-momentum-coupled (SOAM-coupled) spin-1 condensates. At vanishing detuning, a ferromagnetic SOAM-coupled spin-1 Bose-Einstein condensate (BEC) can have two ground-state phases, namely, coreless and polar-core vortex states, whereas an antiferromagnetic BEC supports only polar-core vortex solution. The angular momentum per particle, longitudinal magnetization, and excitation frequencies display discontinuities across the phase boundary between the coreless vortex and polar-core vortex phases. The low-lying excitation spectrum evaluated by solving the Bogoliubov–de Gennes equations is marked by avoided crossings and hence the hybridization of the spin and density channels. The spectrum is further confirmed by the dynamical evolution of the ground state subjected to a perturbation suitable to excite a density or a spin mode and a variational analysis for the density-breathing mode.

DOI: [10.1103/PhysRevA.108.043310](https://doi.org/10.1103/PhysRevA.108.043310)

## I. INTRODUCTION

The experimental realization of spin-orbit (SO) coupling marked an important milestone in the field of quantum degenerate Bose gases [1–3]. The SO coupling in these experiments, coupling the spin and linear momentum of electrically neutral bosons, is created by controlling the interaction between atoms and light [1–4]. The rich ground-state phase diagram of SO-coupled spin-1 Bose-Einstein condensates (BECs), besides having stripe, plane-wave, and zero-momentum phases [5,6], also admits half-quantum vortex [7], vortex-lattice states [8], etc. Apart from the ground-state phase diagram, collective excitations in trapped SO-coupled BECs—another aspect of fundamental interest [9,10]—have been studied experimentally [11,12] as well as theoretically [13,14] in harmonically trapped SO-coupled pseudospinor BECs. Recently, we studied the collective excitations in a quasi-one-dimensional SO-coupled spin-1 BEC with antiferromagnetic interactions at zero and finite temperatures [15].

For the last few years, there has been a growing interest in coupling the orbital angular momentum of atoms' center of mass with their internal spin states using a pair of copropagating Laguerre-Gaussian laser beams with opposite winding numbers. Commonly known as spin-orbital-angular-momentum (SOAM) coupling, this feature has been independently demonstrated by two experimental groups by coupling two [16] or three magnetic sublevels of  $F = 1$  manifold of  $^{87}\text{Rb}$  atoms [17,18], thus affirming the validity

of earlier theoretical proposals [19–24]. There also has been an interest in theoretical models of SOAM coupling inspired by Weyl-type SO coupling [25]. In the context of SOAM-coupled pseudospin-1/2 BECs, polarized and zero-momentum phases have been observed experimentally. Besides these, stripe, annular-stripe, two-vortex molecule, and vortex-antivortex molecule phases have also been studied theoretically [22,26–28]. Theoretical studies on the effects of the ring-trapping potential on the annular-stripe phase in SOAM-coupled pseudospin-1/2 condensate have also been carried out [21,29].

Along with studies on equilibrium ground-state phase diagrams, spectroscopic studies have been carried out on SOAM-coupled pseudospin-1/2 BEC [27,30,31]. In particular, the low-lying excitation spectrum, including breathing and dipole modes, has been studied for the half-skyrmion and vortex-antivortex phases [27,30]. Additionally, the ground-state phases and excitation spectrum have been studied for pseudospin-1/2 BEC with higher-order SOAM coupling [31].

In the experimental realizations of SOAM coupling in the spin-1 spinor BEC of  $^{87}\text{Rb}$  atoms [17,18], a Gaussian and a Laguerre-Gaussian beam copropagating along the  $z$  direction were considered, leading to an orbital angular-momentum transfer of  $\hbar$  to the atoms. Considering a theoretical SOAM-coupling model with an angular-momentum transfer of  $2\hbar$  [23], the ground-state phase diagram and the dynamics ensuing on sudden quench of quadratic Zeeman terms have been studied. The different considerations of angular-momentum transfer to the atoms yield different single-particle Hamiltonians and, consequently, different phase diagrams. In this context, considering the experimentally realized SOAM coupling [17,18], the detailed phase diagrams and excitation spectrums of SOAM-coupled spin-1 BECs with polar and ferromagnetic spin-exchange interactions have not yet been

\*2018phz0003@iitrpr.ac.in

†rajat.19phz0009@iitrpr.ac.in

‡arko@iitmandi.ac.in

§sandeep@iitrpr.ac.in

theoretically studied. To the best of our knowledge, collective excitations of an SOAM-coupled spin-1 BEC have not been studied, irrespective of the theoretical models employed. This sets the stage for the present work. With inspiration drawn from the experimental research reported in Ref. [18] and an aim to bridge the research gap, our objective is to study the excitation spectrum of the ground-state phases observed in SOAM-coupled spin-1 BECs. The excitation spectrum, calculated by solving the Bogoliubov–de Gennes (BdG) equations, is supported by the time evolution of the expectation of the physical observables with an aptly chosen perturbation being added to the Hamiltonian at time  $t = 0$ . For the sake of comprehensiveness, we additionally employ the variational method to analytically calculate the frequency of the density-breathing mode.

The paper is organized as follows. In Sec. II, we present the Hamiltonian describing an SOAM-coupled spin-1 BEC in cylindrical coordinates and the reduction to a quasi-two-dimensional (quasi-2D) formulation through a set of coupled Gross-Pitaevskii equations (GPEs). In Sec. III, we discuss the ground-state phases of SOAM-coupled ferromagnetic and polar BECs in the limit of vanishing detuning. In Sec. IV A, we discuss the spectrum of the noninteracting SOAM-coupled spin-1 BEC, and follow it with the collective excitations of the interacting SOAM-coupled spin-1 BECs in IV B. In Sec. IV C, we explore the effect of detuning on the ground-state phases and excitation spectrum. In Sec. IV D, we study real-time dynamics of the perturbed ground state to illustrate the ensuing dynamics in the density and spin channels. In Sec. IV E, the variational method to study a few low-lying modes is discussed, followed by the summary of key results in Sec. V.

## II. MODEL

In this work, we consider SOAM-coupled spin-1 BECs in which the orbital angular momentum of the center of the mass of the atoms is synthetically coupled to their internal spin states [16,17]. In the cylindrical coordinate system, the noninteracting (single-particle) part of the Hamiltonian for the spinor BEC is [17,18]

$$H_s = \left[ -\frac{\hbar^2}{2M} \frac{\partial}{r \partial r} \left( r \frac{\partial}{\partial r} \right) + \frac{L_z^2}{2Mr^2} - \frac{\hbar^2}{2M} \frac{\partial^2}{\partial z^2} + V(\mathbf{r}) \right] \mathbb{I} + \Omega(r) \cos(\phi) S_x - \Omega(r) \sin(\phi) S_y + \delta S_z, \quad (1)$$

where  $\mathbb{I}$  is a  $3 \times 3$  identity matrix;  $V(\mathbf{r}) = M\omega_0^2 r^2/2 + M\omega_z^2 z^2/2$  constitutes the external harmonic potential to trap the atoms of mass  $M$ ;  $L_z = -i\hbar \partial/\partial \phi$  is the angular momentum operator;  $\Omega(r) = \Omega_0 \sqrt{e}(r/r_0) e^{-r^2/2r_0^2}$  is the Raman-coupling strength with  $\Omega_0$  and  $r_0$  as the Rabi frequency and the radius of the maximum-intensity (cylindrical) surface [17,18], respectively;  $\delta$  is the Raman detuning; and  $S_x$ ,  $S_y$ , and  $S_z$  are irreducible representations of the spin-1 angular momentum operators. Under mean-field approximation, the interacting part of the Hamiltonian  $H_{\text{int}}$  is given by [32]

$$H_{\text{int}} = \frac{c_0}{2} \rho + \frac{c_1}{2} \mathbf{F} \cdot \mathbf{S} \quad (2)$$

with  $c_0$  and  $c_1$  as the mean-field interaction parameters. The total density of the system is given by  $\rho$ ,  $\mathbf{F} = (F_x, F_y, F_z)$  is

the spin-density vector, and  $\mathbf{S} = (S_x, S_y, S_z)$ . Since the SOAM coupling is restricted to the radial plane, and we consider  $\omega_z \gg \omega_0$ , the dominant dynamics is constrained to the same plane with frozen axial degrees of freedom. We can then integrate out the  $z$  degree of freedom from the condensate wave function and describe the system as quasi-2D on the radial  $r$ - $\phi$  plane. Starting from the Hamiltonian  $H = H_s + H_{\text{int}}$ , in polar coordinates, we obtain the following coupled quasi-2D GPEs in dimensionless form:

$$i \frac{\partial \psi_{\pm 1}}{\partial t} = \mathcal{H} \psi_{\pm 1} + c_1 (\rho_0 \pm \rho_-) \psi_{\pm 1} + c_1 \psi_{\mp 1}^* \psi_0^2 \pm \delta \psi_{\pm 1} + \frac{\Omega(r)}{\sqrt{2}} e^{\pm i\phi} \psi_0, \quad (3a)$$

$$i \frac{\partial \psi_0}{\partial t} = \mathcal{H} \psi_0 + c_1 \rho_{\pm} \psi_0 + 2c_1 \psi_{+1} \psi_{-1} \psi_0^* + \frac{\Omega(r)}{\sqrt{2}} (e^{-i\phi} \psi_{+1} + e^{i\phi} \psi_{-1}), \quad (3b)$$

where

$$\mathcal{H} = -\frac{1}{2} \frac{\partial}{r \partial r} \left( r \frac{\partial}{\partial r} \right) + \frac{L_z^2}{2r^2} + \frac{r^2}{2} + c_0 \rho, \quad \rho = \sum_{j=\pm 1,0} \rho_j, \quad \rho_j = |\psi_j|^2, \quad \rho_{\pm} = \rho_{+1} \pm \rho_{-1}. \quad (4)$$

Under geometric renormalization, in terms of  $s$ -wave scattering lengths  $a_0$  and  $a_2$  in the total spin-0 and 2 channels, respectively,  $c_0$  and  $c_1$  take the form

$$c_0 = \sqrt{8\pi\alpha} \frac{N(a_0 + 2a_2)}{3a_{\text{osc}}}, \quad c_1 = \sqrt{8\pi\alpha} \frac{N(a_2 - a_0)}{3a_{\text{osc}}} \quad (5)$$

denoting the spin-independent and spin-dependent interactions, respectively. The anisotropy parameter  $\alpha = \omega_z/\omega_0$  is defined to be the trapping frequency ratio along the axial to the radial direction, and  $N$  is the total number of atoms. The units of length, time, energy, and energy eigenfunctions are considered to be  $a_{\text{osc}} = \sqrt{\hbar/(M\omega_0)}$ ,  $\omega_0^{-1}$ ,  $\hbar\omega_0$ , and  $a_{\text{osc}}^{-1}$ , respectively, and  $\int r \rho(r) dr d\phi = 1$ .

## III. GROUND-STATE QUANTUM PHASES OF SOAM-COUPLED SPINOR BEC

To understand the intercomponent phase relationship imposed by various competing terms in the Hamiltonian, we consider a generic circularly symmetric *ansatz*,  $\psi_j = f_j(r) e^{i(w_j \phi + \beta_j)}$ , for the component wave functions, where  $w_j$  and  $\beta_j$  are, respectively, the phase-winding number and constant phase associated with the radially symmetric real function  $f_j$ . The phase-dependent part of the interaction energy is minimized, provided [33]

$$w_{+1} - 2w_0 + w_{-1} = 0, \quad (6a)$$

$$\beta_{+1} - 2\beta_0 + \beta_{-1} = \begin{cases} 2n\pi & \text{for } c_1 < 0, \\ (2n' + 1)\pi & \text{for } c_1 > 0, \end{cases} \quad (6b)$$

where  $n$  and  $n'$  are integers. Similarly, the SOAM part of the energy is minimized if

$$w_{+1} - w_0 = 1, \quad w_0 - w_{-1} = 1, \quad (7a)$$

$$\beta_{+1} - \beta_0 = (2p + 1)\pi, \quad \beta_0 - \beta_{-1} = (2p' + 1)\pi, \quad (7b)$$

where  $p$  and  $p'$  are again integers. If the conditions on the winding numbers in Eq. (7a) are satisfied, the condition in Eq. (6a) is satisfied too. On the other hand, conditions between the constant phase factors in Eqs. (6b) and (7b) can be simultaneously satisfied for  $c_1 < 0$  only.

To further substantiate the intercomponent phase relationships imposed by SOAM coupling, we extract  $\mathcal{S} = S_x \cos \phi - S_y \sin \phi$  [26] from the single-particle Hamiltonian  $H_s$ . In the limit when  $\Omega_0$  is large, the  $c_1$ -dependent part of the Hamiltonian can be neglected, and the phase structure of the emergent ground-state solution is mainly determined by  $\mathcal{S}$  via its minimum energy eigenspinor. The normalized eigenspinor of  $\mathcal{S}$  with minimum eigenenergy  $-1$  can be written as  $(e^{i(m+1)\phi}, -\sqrt{2}e^{im\phi}, e^{i(m-1)\phi})^T/2$ , with  $m$  being any integer. The phase structure of this eigenspinor is consistent with phase relations in Eqs. (7a) and (7b). With an increase in  $m$ , there is an energy cost from the phase-dependent part of the kinetic energy, suggesting that only small values of phase-winding numbers may emerge. Numerical results confirm this, where we obtain a solution corresponding to  $m = 0$  in large  $\Omega_0$  limit irrespective of the nature of spin-exchange interactions. The spinor part of the ground state in this limit tends to approach the aforementioned eigenstate of  $\mathcal{S}$  with  $m = 0$ .

Various numerical techniques have been employed in the literature to study spinor BECs in quasi-one-dimensional, quasi-two-dimensional, and three-dimensional settings [34–38]. In practice, we choose the finite-difference method and choose different initial guess solutions as an input to Eqs. (3a) and (3b) to arrive at ground-state solutions. As an example, we take initial states  $\Psi \sim e^{-r^2/2} \times (e^{i(m+1)\phi}, -\sqrt{2}e^{im\phi}, e^{i(m-1)\phi})^T/2$ , with different values of  $m$ . Besides these initial states, we consider a random initial guess where  $\psi_j(r)$  are complex Gaussian random numbers.

At the outset, motivated by the experimental realization of the SOAM-coupled BECs [17,18] using spin-1  $^{87}\text{Rb}$  atoms, we validate our numerical simulations to study and emulate the observed ground-state quantum phases of the ferromagnetic system in the absence of detuning  $\delta = 0$  first and later with  $\delta \neq 0$ . It is to be noted that in the experiments [18], both zero and nonzero values of detuning have been considered. Similar to the experiment, we consider the  $^{87}\text{Rb}$  atoms confined in an anisotropic harmonic trap with  $\omega_0 = 2\pi \times 140$  Hz and  $r_0 = 15 \mu\text{m}$  [18]. However, we take  $\omega_z = 2\pi \times 2400$  Hz, enabling us to perform quasi-2D simulations. Here  $a_0 = 101.8a_B$  and  $a_2 = 101.4a_B$ , with  $a_B$  as the Bohr radius [39]. The ground-state densities and phase distributions, obtained numerically by solving the coupled GPEs (3a) and (3b) with imaginary-time propagation, for given  $\Omega_0$  and  $N$ , are in qualitative agreement with the experimental results. The ground-state densities calculated for a pair of  $\Omega_0$  values with  $N = 5000$  are shown in Figs. 1(a) and 1(b). For  $\Omega_0 = 0.25$ , the solutions with  $(+2, +1, 0)$  and  $(0, -1, -2)$  phase-winding numbers are two degenerate ground states, and with  $\Omega_0 = 1$ , the  $(+1, 0, -1)$  state is obtained as the

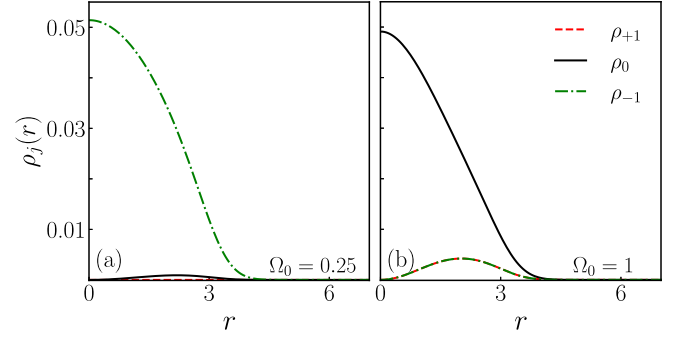


FIG. 1. Ground-state densities of the SOAM-coupled  $^{87}\text{Rb}$  spin-1 BEC with  $c_0 = 121.28$  and  $c_1 = -0.56$  corresponding to  $N = 5000$  for (a)  $\Omega_0 = 0.25$  and (b)  $\Omega_0 = 1$ . The  $j = +1, 0$ , and  $-1$  spin components carry phase-winding numbers of (a)  $+2, +1$ , and  $0$ , respectively, and (b)  $+1, 0$ , and  $-1$ , respectively. As discussed in the text, the various quantities in this and the rest of the figures are dimensionless.

ground-state solution. As we vary  $\Omega_0$  from 0 to 20, at small  $\Omega_0$ , due to the coaction of spin-dependent interaction term and SOAM coupling, a  $(+2, +1, 0)$ -type solution appears as the ground state. After a critical value of coupling strength (say,  $\Omega_0^c$ ),  $\Omega\mathcal{S}$  primarily dictates the nature of the solution to result in a  $(+1, 0, -1)$ -type phase. The condition  $\langle \mathcal{S} \rangle \approx -1$  is satisfied in this latter phase for sufficiently large  $\Omega_0$  as shown in Fig. 2(a), which indicates that no further phase can be expected with higher  $\Omega_0$ . We term these two phases I and II. In contrast to  $^{87}\text{Rb}$ ,  $(+1, 0, -1)$ -type is the single ground-state phase for  $^{23}\text{Na}$  with  $c_1 > 0$ . In this case too,  $\langle \mathcal{S} \rangle \approx -1$  at large  $\Omega_0$  as shown in Fig. 2(a).

Longitudinal magnetization per particle  $f_z = \int F_z d\mathbf{r}$ ; spin expectation per particle  $f = \int |\mathbf{F}| d\mathbf{r}$ , where  $|\mathbf{F}| = \sqrt{F_x^2 + F_y^2 + F_z^2}$ ; and angular momentum per particle  $\langle L_z \rangle$  can be used to characterize these ground-state phases. In the ferromagnetic domain with  $c_0 = 121.28$  and  $c_1 = -0.56$ , for  $\Omega_0 \leq \Omega_0^c = 0.3$ , i.e., in phase I,  $\langle L_z \rangle \neq 0$  and increases continuously as shown in the inset of Fig. 2(a), whereas  $|f_z| \approx 1$  and  $f = 1$  as shown in Fig. 2(b). For  $\Omega_0 > \Omega_0^c$ , the transition to phase II is accompanied by discontinuities in  $\langle L_z \rangle$ ,  $|f_z|$ , and  $f$ ; whereas the former two reduce to zero, the latter becomes less than one. In the antiferromagnetic domain, e.g., with

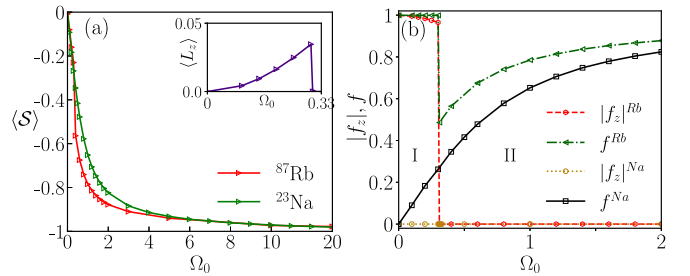


FIG. 2. (a)  $\langle \mathcal{S} \rangle$  as a function of SOAM-coupling strength  $\Omega_0$  for  $^{87}\text{Rb}$  with  $c_0 = 121.28$  and  $c_1 = -0.56$  and  $^{23}\text{Na}$  with  $c_0 = 121.35$  and  $c_1 = 3.80$ . Inset in (a):  $\langle L_z \rangle$  for  $^{87}\text{Rb}$  as a function of  $\Omega_0$ . (b)  $|f_z|$  and  $f$  for  $^{87}\text{Rb}$  and  $^{23}\text{Na}$  as a function of SO coupling strength  $\Omega_0$ . The  $c_0$  and  $c_1$  for  $^{87}\text{Rb}$  and  $^{23}\text{Na}$  are the same as those in (a).

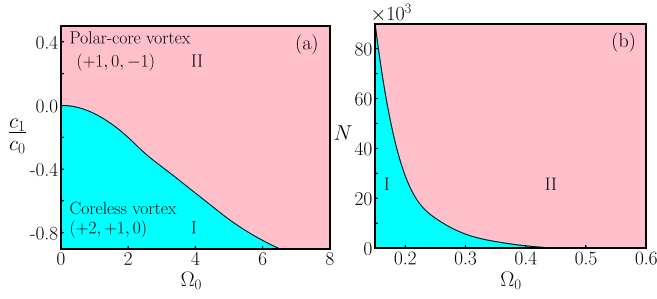


FIG. 3. The ground-state phase diagrams in (a)  $c_1/c_0$ - $\Omega_0$  and (b)  $N$ - $\Omega_0$  planes. In (a)  $c_0$  was kept fixed at 121.28 while varying  $c_1$ . In (b)  $c_1/c_0 = -0.0046$  corresponding to  $^{87}\text{Rb}$ .

$c_0 = 121.35$  and  $c_1 = 3.8$ , there is no phase transition with an increase in  $\Omega_0$ , resulting in smooth behavior of the same quantities. Here  $f$  asymptotically approaches one, whereas  $|f_z|$  and  $\langle L_z \rangle$ , expectantly, remain zero.

Furthermore, we calculate the ground-state phase diagrams in the  $c_1/c_0$ - $\Omega_0$  plane, where we fix  $c_0 = 121.28$  and vary  $c_1$ , and the  $N$ - $\Omega_0$  plane for fixed  $c_1/c_0 = -0.0046$ , which corresponds to  $^{87}\text{Rb}$ . The ratio  $c_1/c_0$  may be manipulated experimentally by tuning one of the scattering lengths by optical Feshbach resonance [40]. These two are respectively shown in Figs. 3(a) and 3(b), thus again illustrating that an antiferromagnetic BEC has one ground-state phase in contrast to the ferromagnetic one. It can be seen that with a decrease in  $c_1$  (keeping  $c_0$  fixed) in the ferromagnetic phase, the domain of phase I increases, whereas with an increase in the number of atoms (keeping  $c_1/c_0$  fixed), it decreases. Phases I and II also have distinctive topological spin textures  $\mathbf{F} = (F_x, F_y, F_z)$ . For the solutions in Figs. 1(a) and 1(b), spin-textures are shown in Figs. 4(a) and 4(b), respectively. The spin-textures in Figs. 4(a) and 4(b) are in agreement with those reported in Ref. [18]; at the center,  $\mathbf{F}$  points along negative  $z$  direction in Fig. 4(a), whereas it is zero in Fig. 4(b). The details of the spin textures allow the identification of phases I and II with the coreless vortex and polar-core vortex states, respectively. It is to be noted in Ref. [23] that the two reported circularly symmetric phases correspond to  $(-4, -2, 0)$ - and

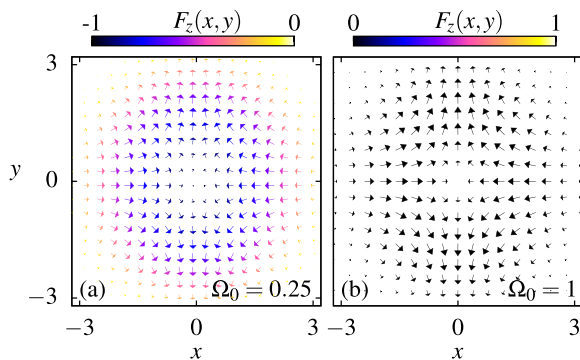


FIG. 4. (a and b) Spin texture for 5000 atoms of  $^{87}\text{Rb}$  system with the coupling strength  $\Omega_0 = 0.25$  and  $\Omega_0 = 1$ , respectively. The length of the arrows shows the projection of  $\mathbf{F}(x, y)$  on the  $x$ - $y$  plane, and the color bar indicates its component along the  $z$  axis;  $\mathbf{F}(x, y)$  vector field lies on the  $x$ - $y$  plane in (b).

$(-2, 0, +2)$ -type solutions, which are different from phases I and II in the present work.

#### IV. COLLECTIVE EXCITATION SPECTRUM

To study the excitation spectrum, we exploit the innate circular symmetry of the Hamiltonian. To this end, we perform a local spin rotation about  $\hat{z}$  by the azimuthal angle  $-\phi$  to remove the  $\phi$  dependence from the Hamiltonian. As a result, the order parameter  $\Psi = (\psi_{+1}, \psi_0, \psi_{-1})^T$  is transformed to  $e^{-iS_z\phi}\Psi = (e^{-i\phi}\psi_{+1}, \psi_0, e^{i\phi}\psi_{-1})^T$ , and the transformed Hamiltonian takes the form

$$H = \left[ -\frac{1}{2} \frac{\partial}{\partial r} \left( r \frac{\partial}{\partial r} \right) + \frac{(L_z + S_z)^2}{2r^2} + V(r) \right] \mathbb{I} + \Omega(r) S_x + H_{\text{int}}, \quad (8)$$

where  $H_{\text{int}} = c_0\rho/2 + c_1\mathbf{F} \cdot \mathbf{S}/2$ . The Hamiltonian in Eq. (8) is circularly symmetric, and one can seek the simultaneous eigenfunctions of  $H$  and  $L_z$  with fixed angular momentum  $l_z = 0, 1, \dots$ . For example, the solutions presented in Figs. 1(a) and 1(b) can now be seen as corresponding to  $l_z = 1$  and 0, respectively. The single-particle Hamiltonian in Eq. (1) is symmetric under the transformation defined by an operator  $\mathcal{R} = \exp(-iS_x\pi)K$ , where  $K$  is the complex-conjugation operator. This implies that for any  $l_z \neq 0$ , there will be two degenerate solutions connected  $\mathcal{R}$ . For example, for  $l_z = 1$ , the degenerate counterpart with  $l_z = -1$  corresponds to  $(0, -1, -2)$  phase-winding numbers in the component wave functions.

We use the Bogoliubov approach to study the excitation spectrum, in which we consider the fluctuations to the ground state by writing the perturbed order parameter as

$$\Psi(r, \phi, t) = e^{-i\mu t + i(l_z + S_z)\phi} [\Psi_{\text{eq}}(r) + \delta\Psi(r, t)e^{il_q\phi}], \quad (9)$$

where  $\Psi_{\text{eq}}(r) = [R_{+1}(r), R_0(r), R_{-1}(r)]^T$  is the radial part of the order parameter with  $R_j$  as the radial wave function corresponding to the  $j$ th spin component,  $\mu$  is the chemical potential, and  $l_q = 0, \pm 1, \pm 2, \dots$  is the magnetic quantum number associated with the angular momentum of the quasi-particle excitations. The details of the BdG analysis are given in the Appendix.

##### A. Noninteracting system

To understand the effect of coupling strength, we first study the single-particle excitation spectrum. The ground-state solution has phase-winding numbers  $(\pm 1, 0)$  in  $j = \pm 1, 0$  spin states, respectively. The excitation spectrum is shown in Fig. 5. For  $\Omega_0 = 0$ , the  $n$ th energy level is  $3(n+1)$ -fold degenerate, as the single-particle Hamiltonian is identical with a system of three decoupled isotropic two-dimensional harmonic oscillators. For example, excitations with energies 0 and 1 are three- and sixfold degenerate, respectively. The SOAM-coupling lifts the degeneracies partially. For example, for  $\Omega_0 \neq 0$ , there is only one zero-energy excitation; similarly, the red lines in the spectrum in Fig. 5 correspond to nondegenerate excitations, whereas the black ones to twofold degenerate modes. The nondegenerate modes have the magnetic quantum number of the excitation  $l_q = 0$ , whereas modes with twofold degeneracy have  $l_q \neq 0$ .



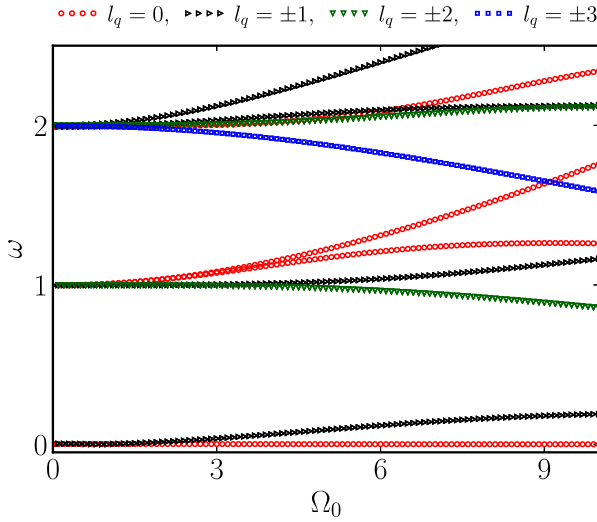


FIG. 5. Single-particle excitation spectrum for spin-1 BEC as a function of SOAM coupling strength  $\omega_0$ .

**B. Interacting spin-1 BEC**

Here we study the excitation spectrum (a) as a function of  $\Omega_0$  for fixed  $c_0$  and  $c_1$  and (b) as a function of  $N$  for fixed  $\Omega_0$  and  $c_0/c_1$  ratio. Both  $\Omega_0$  and  $N$  can be varied in an experiment [17,18]. As was discussed in Sec. III, for  $c_1 < 0$ , both phases I and II can appear as the ground-state phases with a variation of either  $\Omega_0$  or  $N$ . We primarily consider  $^{87}\text{Rb}$  BEC in the following discussion.

*Phase I:* Here we consider  $c_0 = 121.18$  and  $c_1 = -0.56$  and vary  $\Omega_0$ . The excitation spectrum for phase I is shown in Fig. 6(a) for  $l_q = 0, \pm 1$  and (b) for  $|l_q| \geq 2$ . The modes with frequencies 1 and 2 are, respectively, dipole and density-breathing modes in Fig. 6(a). This identification of a mode is based on the real-time evolution of the expectation of a suitably chosen observable, as will be discussed in the next subsection. The presence of ferromagnetic interactions further aids the lifting of the degeneracy, in this case between the modes with magnetic quantum numbers  $\pm l_q$ , which are degenerate at the single-particle level. We have confirmed this, for example, by examining the excitation spectrum of a system with  $c_0 = 121.18$  and  $c_1 = -0.6c_0 \ll -0.56$  (not shown here), where the nondegenerate nature of the spectrum is clearly seen. In phase I, there are two zero-energy Goldstone modes corresponding to two broken continuous symmetries, namely, gauge and rotational symmetry. The latter corresponds to the symmetry transformation generated by  $L_z$ .

*Phase II:* As already mentioned in Sec. III, the transition from phase I to phase II occurs at  $\Omega_0 > 0.3$  for  $c_0 = 121.18$  and  $c_1 = -0.56$ . The transition is accompanied by the discontinuities in the excitation spectrum. The excitation spectrum for phase II is shown in Fig. 6(c). Here among the low-lying modes are dipole and breathing modes corresponding to both density and spin channels. Both density- and spin-dipole modes are doubly degenerate corresponding to magnetic quantum number  $l_q = \pm 1$ . On the other hand, both density- and spin-breathing modes are nondegenerate with  $l_q = 0$ . At small values of  $\Omega_0$ , the energies of the spin

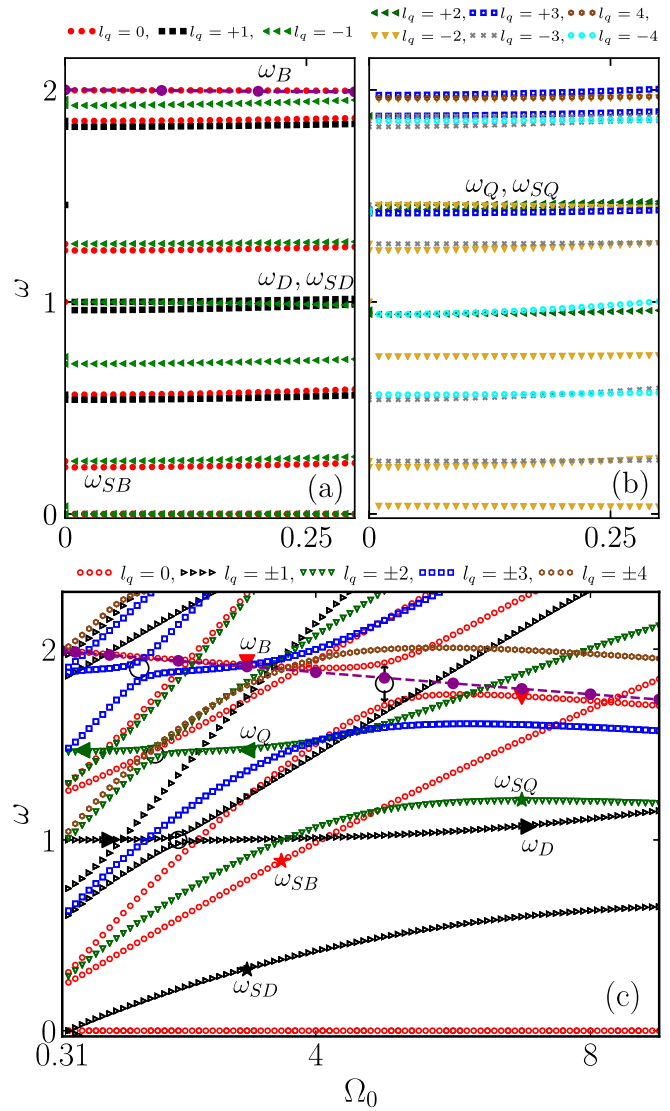


FIG. 6. Low-lying excitation spectrum of  $^{87}\text{Rb}$  SOAM-coupled spin-1 BEC with  $c_0 = 121.18$  and  $c_1 = -0.56$  as a function of coupling strength  $\Omega_0$  of phase I with (a)  $l_q = 0, \pm 1$  and (b)  $l_q = \pm 2, \pm 3, \pm 4, \dots$ ; among the named modes,  $l_q = 0$  for density- and spin-breathing,  $l_q = +1$  for density-dipole,  $l_q = -1$  for spin-dipole,  $l_q = +2$  for density-quadrupole, and  $l_q = -2$  for spin-quadrupole modes. (c) The same for phase II, where  $l_q = 0$  for density- and spin-breathing,  $l_q = \pm 1$  for density- and spin-dipole,  $l_q = \pm 2$  for density- and spin-quadrupole modes. In (a) and (c), the dashed magenta line is the variational estimate for the density-breathing mode.

modes are less than their density-mode analogues. There is a single zero-energy mode due to the broken gauge symmetry in this phase. Besides these modes, the density- and spin-quadrupole modes, are also marked in the excitation spectrum in Figs. 6(a)–6(c). As the collective excitations characterize a systems response to small perturbations, these can be experimentally studied using Bragg spectroscopy [11,12].

Additionally, the variation in SOAM-coupling strength leads to avoided crossings between the pairs of excitations, a few of which are identified by the black circles in Fig. 6(c). We observe that the avoided crossing occurs between the

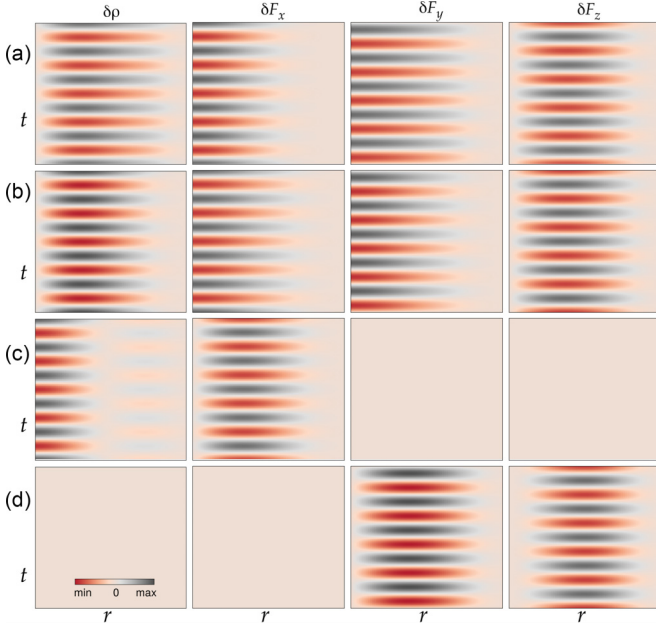


FIG. 7. (a) Density fluctuations,  $\delta\rho(r, \phi = 0, t)$ , and spin-density fluctuations,  $\delta F_\nu(r, \phi = 0, t)$ , with  $\nu = x, y, z$  corresponding to  $\omega_D = 1$ . (b–d) The same for  $\omega_{SD} = 0.08$ ,  $\omega_B = 1.97$ , and  $\omega_{SB} = 0.37$ , respectively. The radial and time extents, along the horizontal and vertical directions, respectively, in each subfigure are  $4a_{osc}$  and  $5T$ , respectively, where  $T = 2\pi/\omega$  is the time period of the corresponding mode with  $\omega$  frequency. The presence of both density and spin fluctuations in (a)–(c) is an outcome of the avoided crossing between the pairs of modes in the excitation spectrum shown in Fig. 6(c).

density and spin oscillations associated with the same magnetic quantum number  $l_q$ . In the vicinity of the avoided crossing, the roles of the density and spin modes are interchanged as shown in Fig. 6(c). We study this mode mixing by examining the density ( $\delta\rho$ ) and spin fluctuations ( $\delta F_x, \delta F_y, \delta F_z$ ) yielded by the perturbed order parameter and defined as

$$\delta\rho = 2\text{Re} \sum_j \psi_j \delta\psi_j^*, \quad (10a)$$

$$\delta F_x = \sqrt{2}\text{Re}(\psi_{+1}\delta\psi_0^* + \psi_0\delta\psi_{+1}^* + \psi_{-1}\delta\psi_0^* + \psi_0\delta\psi_{-1}^*), \quad (10b)$$

$$\delta F_y = -\sqrt{2}\text{Im}(-\psi_{+1}\delta\psi_0^* + \psi_0\delta\psi_{+1}^* + \psi_{-1}\delta\psi_0^* - \psi_0\delta\psi_{-1}^*), \quad (10c)$$

$$\delta F_z = 2\text{Re}(\psi_{+1}\delta\psi_{+1}^* - \psi_{-1}\delta\psi_{-1}^*), \quad (10d)$$

where Re and Im denote the real and imaginary part, respectively. For a pure density mode, one would expect that  $\delta\rho \neq 0$  and  $\delta F_\nu = 0$ ; similarly, for a pure spin mode, one would expect that  $\delta\rho = 0$  and at least one of the  $\delta F_\nu \neq 0$ . The order-parameter fluctuation  $\delta\Psi(r, \phi, t)$ , and hence density and spin fluctuations, can be constructed with the Bogoliubov quasiparticle amplitudes  $u$  and  $v$  corresponding to the frequency  $\omega$  of the mode as  $\delta\psi_j(r, \phi, t) \propto e^{i(l_z + j + l_q)\phi} [u_j(r)e^{-i\omega t} - v_j^*(r)e^{i\omega t}]$ . In the excitation spectrum in Fig. 6(c) at  $\Omega_0 = 1$ , the density- and spin-dipole modes'

frequencies are  $\omega_D = 1$  and  $\omega_{SD} = 0.08$ , respectively, and the density- and spin-breathing modes' frequencies are  $\omega_B = 1.97$  and  $\omega_{SB} = 0.37$ , respectively. One can see that the density-dipole, density-breathing, and spin-dipole modes encounter avoided crossings, whereas the spin-breathing mode does not. This observation agrees with the density and spin-density fluctuations evaluated along the  $\phi = 0$  line and shown in Figs. 7(a)–7(d). For the density-dipole mode with  $\omega_D = 1$ , both density and spin channels are excited as is seen from  $\delta\rho(r, \phi = 0, t)$  and  $\delta F_\nu(r, \phi = 0, t)$  in Fig. 7(a), where  $\nu = x, y, z$ . Similarly, number density, longitudinal ( $F_z$ ), and transverse magnetization ( $F_x, F_y$ ) densities oscillate in time, corresponding to the spin-dipole mode in Fig. 7(b), and density-breathing mode ends up exciting both the number and transverse magnetization densities in Fig. 7(c). On the other hand, the spin-breathing mode excites the spin channel alone in Fig. 7(d). The density- and spin-quadrupole modes too excite both the density and spin fluctuations, which are not shown. This mode mixing indicated by both density and spin fluctuations is absent in quasi-one-dimensional SO-coupled BECs where any collective excitation yields either density or spin fluctuations [15]. The nomenclature of the modes in Figs. 6(a)–6(c) is consistent with the density,  $\delta\rho(x, y, t)$ , and longitudinal magnetization density,  $\delta F_z(x, y, t)$ , fluctuations

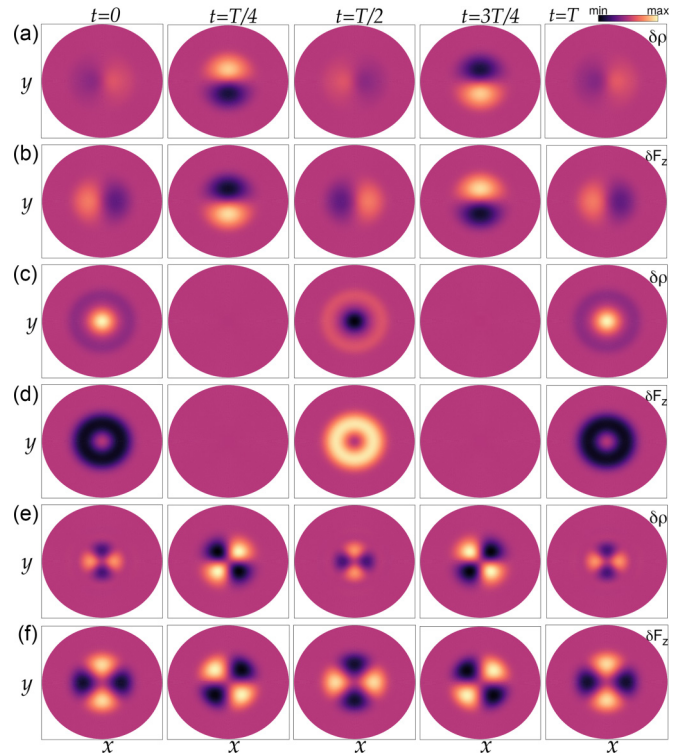


FIG. 8. Density and longitudinal magnetization density fluctuations at  $t = 0, T/4, T/2, 3T/4$ , and  $T$ , where  $T = 2\pi/\omega$  with  $\omega$  as the mode frequency: (a)  $\delta\rho(x, y, t)$  for the density-dipole mode with  $\omega_D = 1$ , (b)  $\delta F_z(x, y, t)$  for the spin-dipole mode with  $\omega_{SD} = 0.08$ , (c)  $\delta\rho(x, y, t)$  for the density-breathing mode with  $\omega_B = 1.97$ , (d)  $\delta F_z(x, y, t)$  for the spin-breathing modes with  $\omega_{SB} = 0.37$ , (e)  $\delta\rho(x, y, t)$  for the density-quadrupole mode with  $\omega_Q = 1.46$ , and (f)  $\delta F_z(x, y, t)$  for the spin-quadrupole mode with  $\omega_{SQ} = 0.46$ . The box size in each subfigure is  $6.4a_{osc} \times 6.4a_{osc}$ .

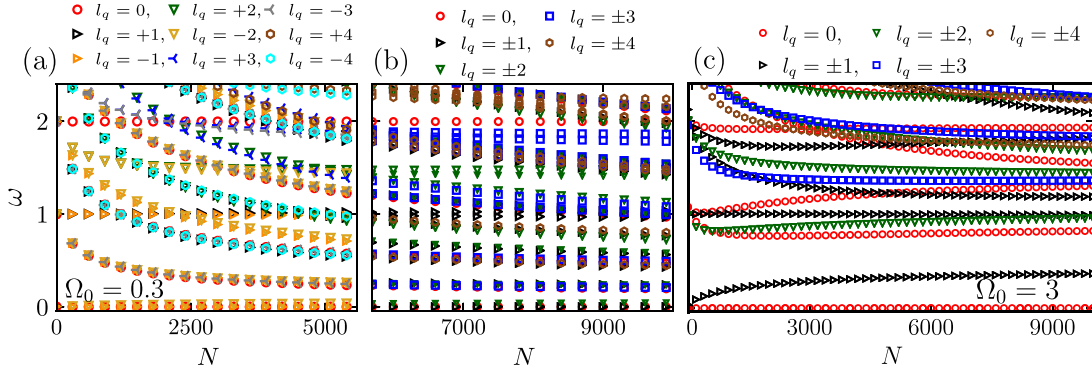


FIG. 9. Low-lying excitation spectrum for  $^{87}\text{Rb}$  spin-1 BEC with  $c_1/c_0 = -0.0046$  as a function of the number of atoms  $N$ : (a and b) for  $\Omega_0 = 0.3$  with a phase transition from phase I to II at  $N = 5700$  and (c)  $\Omega_0 = 3$ . (a) corresponds to the spectrum of phase I, whereas (b) and (c) correspond to the spectrum of phase II. The different point styles in (a) signify nondegenerate modes with different  $l_q$ , while in (b) and (c), red circles, black right-pointing triangles, green down-pointing triangles, and blue squares correspond, respectively, to the modes with  $l_q = 0, \pm 1, \pm 2, \pm 3$ , and so on.

corresponding to density, breathing, and quadrupole modes in Fig. 8 shown at  $t = 0, T/4, T/2, 3T/4$ , and  $T$  instants, where  $T$  is the period of the collective excitation.

Next, we study the excitation spectrum as a function of  $N$  for  $c_1/c_0 = -0.0046$ . Here first, we fix  $\Omega_0$  to 0.3, where a phase transition from phase I to II occurs at  $N = 5700$ . The excitation spectrum, in this case, for phases I and II are shown in Figs. 9(a) and 9(b). The same for  $\Omega_0 = 3$  is shown in Fig. 9(c), where phase II is the ground-state phase with no phase transition. The modes in phase II are, again, either nondegenerate or with twofold degeneracy. For SOAM-coupled  $^{23}\text{Na}$  BEC with  $c_0 = 121.35$  and  $c_1 = 3.8$  the excitation spectrum, which is not shown here, is similar to the spectrum in Fig. 9(c), with some quantitative differences attributable to different  $c_1$  values.

**C. Nonzero detuning**

In this subsection, we consider the effects of the detuning on the phase diagram and excitation spectrum. In Fig. 10, we show the phase diagram in the number of atoms versus the detuning ( $N$ - $\delta$ ) plane for a constant coupling strength of  $\Omega_0 = 5$  and  $c_1/c_0 = -0.0046$  corresponding to  $^{87}\text{Rb}$ . We observe that for a small value of  $\delta$ , the polar-core vortex

(phase II) emerges as the ground-state solution. However, at a critical detuning  $\delta_c$ , a phase transition from (+1,0,-1)-type solution (phase II) to (+2, +1,0)-type solution (phase I) occurs. For example, for  $\Omega_0 = 5$  and  $N = 5000$  corresponding to  $c_0 = 121.18$ ,  $c_1 = -0.56$ , the phase transition occurs at  $\delta_c = 0.3$ . Phase II at smaller detuning and phase I at larger detuning values in Fig. 10 is in qualitative agreement with the experimental findings [18]. It is worth noting that the presence of  $\delta$  in the Hamiltonian leads to the breakdown of the symmetry defined by  $\mathcal{R}$ . As a result, (+2, +1,0) and (0,-1,-2)-type solutions corresponding to  $l_z = 1$  and  $-1$ , respectively, are no longer degenerate. To illustrate the effect of detuning on the excitation spectrum, we contrast the collective excitation spectrum of the condensate with  $N = 5000$ ,  $\Omega_0 = 5$  for (a)  $\delta = 0$  and (b)  $\delta = 0.2$ . The ground-state phase in both these cases is phase II, as can be seen from the phase diagram in Fig. 10. The excitation frequencies as a function of  $l_q$  for these two cases are shown in Figs. 11(a) and 11(b). As discussed in the Appendix, the presence of detuning leads to the lifting of the degeneracies in the excitation spectrum about  $l_q = 0$ . The low-lying modes have been identified in Figs. 11(a) and 11(b). In Fig. 11(a), the density-dipole, spin-dipole, density-quadrupole, and spin-quadrupole exhibit

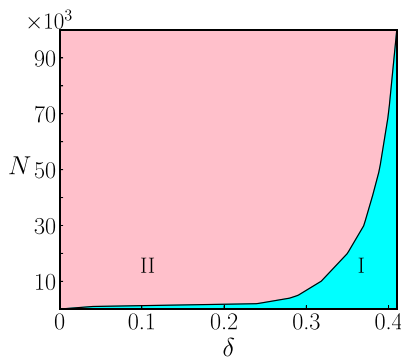


FIG. 10. The ground-state phase diagrams in the  $N$ - $\delta$  plane for  $c_1/c_0 = -0.0046$  corresponding to  $^{87}\text{Rb}$  spin-1 BEC and  $\Omega_0 = 5$ .

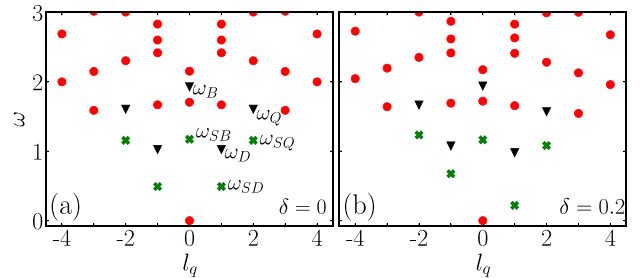


FIG. 11. Collective excitation spectrum for ferromagnetic  $^{87}\text{Rb}$  spin-1 BEC with interaction parameters  $c_0 = 121.28$ ,  $c_1 = -0.56$ , and coupling strength  $\Omega_0 = 5$  for (a)  $\delta = 0$  and (b)  $\delta = 0.2$ . The black down-pointing triangles and green crosses denote the density and spin modes, respectively.



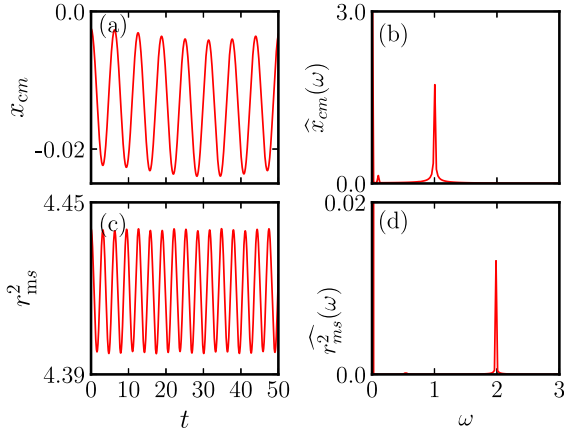


FIG. 12. (a) Center-of-mass oscillations, i.e.,  $x_{\text{cm}}(t)$ , as a function of time and (b) corresponding Fourier transform with a dominant peak at  $\omega = 1$  for  $^{87}\text{Rb}$  spin-1 BEC with  $c_0 = 121.28$ ,  $c_1 = -0.56$ , and  $\Omega_0 = 1$ . (c) Oscillations in the mean square size of the system  $r_{\text{ms}}^2(t)$  and (d) corresponding Fourier transform with a dominant peak at  $\omega = 1.99$  for the same interaction and coupling strengths.

twofold degeneracies corresponding to  $\pm l_q$ . However, in the presence of  $\delta$ , all these modes become nondegenerate and are highlighted in Fig. 11(b).

#### D. Dynamics

We examine the nature of low-lying collective excitations through the time evolution of the expectation of physical observables, which also serves to validate our calculation of the excitation spectrum from BdG equations. Here, we consider the Hamiltonian with an appropriately chosen time-independent perturbation, say,  $H'_s$  added to its single-particle part  $H_s$ . This modifies the coupled GP Eqs. (3a) and (3b) with an added term corresponding to  $H'_s \Psi(r, \phi, t)$  in each equation. We then solve these resultant GPEs over a finite period of time by considering previously obtained ground-state solutions as the initial solutions at  $t = 0$ . Numerically, one needs to consider a two-dimensional spatial grid over here, for which we choose the Cartesian  $x$ - $y$  grid.

We consider  $c_0 = 121.28$ ,  $c_1 = -0.56$ , and  $\Omega_0 = 1$ , which yielded the ground-state phase in Fig. 1(b), as an example set of parameters to study the dynamics. To excite the density-dipole mode, we take the perturbation  $H'_s = \lambda x$ , where  $\lambda \ll 1$ . We then examine the dynamics of the center of mass of the BEC via  $x_{\text{cm}}(t) = \langle x \rangle = \sum_{j=\pm 1,0} \int x \rho_j(x, y, t) dx dy$ , which is plotted in Fig. 12(a). We also compute its Fourier transform  $\hat{x}_{\text{cm}}(\omega)$  to demonstrate that the dominant frequency resonates at  $\omega = 1$  as can be seen in Fig. 12(b) and matches with  $\omega_D = 1$  in the BdG spectrum in Fig. 6(c). We could have chosen  $H'_s = \lambda y$  and then calculated  $y_{\text{cm}}(t)$ , giving us the same excitation frequency. This is a consequence of the twofold degeneracy in the density-dipole mode. We have checked that this mode can also be excited by shifting the minima of the external trapping potential. This particular way of exciting this mode has direct relevance from an experimental point of view, where the minima of potential can be easily shifted. Simi-

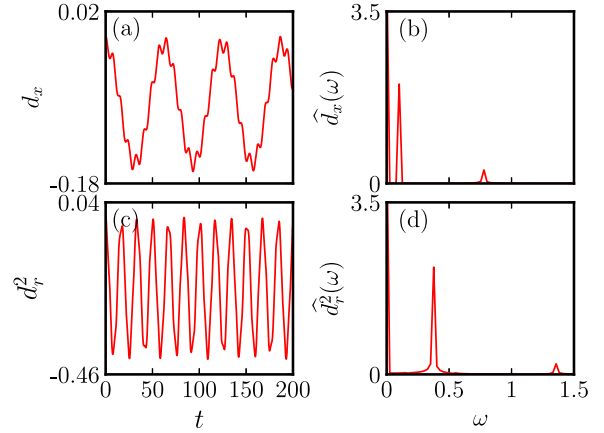


FIG. 13. (a)  $d_x(t)$  as a function of time and (b) corresponding Fourier transform with a dominant peak at  $\omega = 0.1$  for  $^{87}\text{Rb}$  spin-1 BEC with  $c_0 = 121.28$ ,  $c_1 = -0.56$ , and  $\Omega_0 = 1$ . (c)  $d_r^2(t)$  and (d) its Fourier transform with a dominant peak at  $\omega = 0.37$  for the same interaction and coupling strengths.

larly, to examine the excitation of the density-breathing mode with  $H'_s = \lambda(x^2 + y^2)$ , where the relevant observable is  $r^2 = x^2 + y^2$ , we calculate mean square radius  $r_{\text{ms}}^2(t) = \langle r^2 \rangle$  as a function of time, which is plotted in Fig. 12(c). The Fourier transform  $\hat{r}_{\text{ms}}^2(\omega)$  of  $r_{\text{ms}}^2(t)$  reveals a dominant peak at  $\omega = 1.99$  in Fig. 12(d) which is close to the BdG result of  $\Omega_B = 1.97$ . This mode, again, can be excited by perturbing the trap strength, which can be achieved in an experiment with ease, thus giving access to this mode. Similarly, the spin-dipole mode can be excited by adding a perturbation  $H' = \lambda x S_z$  or  $\lambda y S_z$  with  $x S_z$  or  $y S_z$  as the pertinent observable corresponding to the spin-dipole mode. The two possible observables again reflect the twofold degeneracy of spin-dipole modes. The time variation of  $d_x(t) = \langle x S_z \rangle = \sum_{j=\pm 1, -1} \int x \rho_j(x, y, t) dx dy$  is shown in Fig. 13(a) and its Fourier transform in Fig. 13(b) has a dominant peak at  $\omega = 0.1$ , which corresponds to the spin-dipole mode labeled in Fig. 6(c) with  $\omega_{\text{SD}} = 0.08$ . Similarly, the spin-breathing mode corresponds to observable  $r^2 S_z$ . In Figs. 13(c) and 13(d), we show the dynamics of  $d_r^2(t) = \langle r^2 S_z \rangle$ , i.e., the relative difference in the mean-square radii of the  $j = \pm 1$  components and the associated Fourier transform, respectively, with a dominant peak at  $\omega = 0.37$ , in agreement with  $\omega_{\text{SB}}$  in Fig. 6(c). The very small secondary peaks present in Figs. 12(b) and 12(d) correspond to the spin-dipole and spin-breathing modes, respectively. These peaks become prominent when subjected to appropriate perturbations and are observed through relevant observables, as shown in Fig. 13. Likewise, the small peaks appearing in Figs. 13(b) and 13(d) also signify modes present in the BdG spectrum. Finally, the density- and spin-quadrupole modes' frequencies calculated from the time evolution of  $\langle xy \rangle$  and  $\langle xy S_z \rangle$  are in agreement with the numbers in Fig. 6(c).

#### E. Variational analysis

For an SOAM-coupled spin-1 system, a few low-lying modes can be studied using a time-dependent variational method [41]. For example, to calculate the density-breathing mode in the absence of detuning, we consider the following



variational ansatz:

$$\Psi = \frac{r}{2\sqrt{\pi}\sigma(t)^2} \exp\left[-\frac{r^2}{2\sigma(t)^2} + i\alpha(t)r^2\right] \times \begin{pmatrix} e^{i(m+1)\phi} \\ -\sqrt{2}e^{im\phi} \\ e^{i(m-1)\phi} \end{pmatrix}, \quad (11)$$

where  $\sigma(t)$  and  $\alpha(t)$  are time-dependent variational parameters used to denote the width of condensate and chirp of Gaussian pulse, respectively, and  $m = \pm 1$  for phase I or 0 for phase II. The Lagrangian of the system is given by

$$L = \sum_j \int dr d\phi \frac{i}{2} \left( \psi_j^* \frac{\partial \psi_j}{\partial t} - \psi_j \frac{\partial \psi_j^*}{\partial t} \right) - E, \quad (12)$$

where energy  $E$  is defined as

$$\begin{aligned} E = \iint \left[ \sum_j \psi_j^* \left\{ -\frac{1}{2r} \frac{\partial}{\partial r} \left( r \frac{\partial}{\partial r} \right) + \frac{L_z^2}{2r^2} + \frac{r^2}{2} \right\} \psi_j \right. \\ + \frac{c_0}{2} \rho^2 + \frac{c_1}{2} (\rho_{+1} + \rho_0 - \rho_{-1}) \rho_{+1} \\ + \frac{c_1}{2} (\rho_{+1} + \rho_{-1}) \rho_0 + \frac{c_1}{2} (\rho_{-1} + \rho_0 - \rho_{+1}) \rho_{-1} \\ + \sqrt{2} \Omega(r) \text{Re}(\psi_{+1}^* e^{i\phi} \psi_0 + \psi_{-1}^* e^{-i\phi} \psi_0) \\ \left. + 2c_1 \text{Re}(\psi_{-1}^* \psi_0^2 \psi_{+1}^*) \right] dr d\phi. \end{aligned} \quad (13)$$

For  $m = \pm 1$ , the (coupled) Euler-Lagrange equations are

$$\begin{aligned} \sigma \dot{(\sigma)} = \frac{\sigma}{2} \left( \frac{6\sqrt{2\pi} \sqrt{e} \Omega_0 \sqrt{\frac{1}{r_0^2} + \frac{2}{\sigma_0^2}} (r_0^7 - 2r_0^5 \sigma_0^2)}{(2r_0^2 + \sigma_0^2)^4} - 2 \right) \\ + \frac{c_0 + c_1 + 10\pi}{8\pi \sigma^3}, \end{aligned} \quad (14a)$$

$$\alpha = \frac{\dot{\sigma}}{2\sigma}, \quad (14b)$$

where “ $\dot{\phantom{x}}$ ” denotes the time derivative. The equilibrium width  $\sigma_0$  of the condensate satisfies

$$\frac{c_0 + c_1 + 10\pi}{4\pi \sigma_0^4} + \frac{6\sqrt{2\pi} \sqrt{e} \Omega_0 \sqrt{\frac{1}{r_0^2} + \frac{2}{\sigma_0^2}} (r_0^7 - 2r_0^5 \sigma_0^2)}{(2r_0^2 + \sigma_0^2)^4} = 2.$$

The frequency of the oscillation in width calculated by linearizing Eq. (14a) about equilibrium width  $\sigma_0$  is

$$\begin{aligned} \omega_B^I = \left[ \frac{15\sqrt{2\pi} r_0^4 \sqrt{e} \Omega_0 (3r_0^2 - 2\sigma_0^2) \sqrt{2r_0^2 + \sigma_0^2} + 1}{(2r_0^2 + \sigma_0^2)^5} \right. \\ \left. + \frac{3(c_0 + c_1 + 10\pi)}{8\pi \sigma_0^4} \right]^{1/2}. \end{aligned} \quad (15)$$

Similarly, for  $m = 0$  in Eq. (11), the density breathing mode is

$$\begin{aligned} \omega_B^{II} = \left[ \frac{15\sqrt{2\pi} r_0^4 \sqrt{e} \Omega_0 (3r_0^2 - 2\sigma_0^2) \sqrt{2r_0^2 + \sigma_0^2} + 1}{(2r_0^2 + \sigma_0^2)^5} \right. \\ \left. + \frac{3(c_0 + c_1 + 6\pi)}{8\pi \sigma_0^4} \right]^{1/2}. \end{aligned} \quad (16)$$

The variationally calculated density-breathing mode's frequency agrees with the values in the BdG spectrum as demonstrated in Figs. 6(a) and 6(c) for phases I and II, respectively. As mentioned in Sec. IV D, the density-breathing mode can be easily excited by modulating the trapping potential strength in an experiment.

## V. SUMMARY AND CONCLUSIONS

We have investigated the low-lying collective excitations of the coreless vortex and the polar-core vortex phases supported by the spin-1 BECs with SOAM coupling. The existence of the two phases is seen in the full phase diagrams in the *ratio of interaction strengths* versus *coupling strength* and also the *number of atoms* versus *coupling strength* planes. We have studied the excitation spectrum as a function of two experimentally controllable parameters, namely, coupling strength and the number of atoms. The excitation spectrums are characterized by the discontinuities across the phase boundary between the two phases and within a phase by avoided crossings between the modes with the same magnetic quantum number of excitations. The avoided crossings signal the hybridization of the density and spin channels; the nature of spin and density fluctuations has indeed confirmed this. Among the low-lying modes, we identify dipole, breathing, and quadrupole modes for density and spin channels. The frequencies of these named modes are further validated from the time evolution of the expectations of the physical observables when an apt time-independent perturbation is added to the system's Hamiltonian. An analytic estimate for the density-breathing modes has also been obtained using the variational analysis. Our results can serve as a benchmark to compute the finite-temperature phase diagram and spin dynamics. With the experimental observation of collective excitation, dispersion (excitation energies as a function of wave number) in Raman-induced SO-coupled BECs [11,12], we expect that our results can also be verified in future SOAM-coupled experiments. With the advent of box-trapping potential [42], an interesting future direction could be to study an SOAM-coupled BEC in such a trap with no rotational symmetry.

## ACKNOWLEDGMENTS

A.R. acknowledges the support of the Science and Engineering Research Board (SERB), Department of Science and Technology, Government of India, under Project No. SRG/2022/000057 and IIT Mandi seed-grant funds under Project No. IITM/SG/AR/87. A.R. acknowledges National Supercomputing Mission (NSM) for providing computing resources of PARAM Himalaya at IIT Mandi, which is implemented by C-DAC and supported by the Ministry of Electronics and Information Technology (MeitY) and Department of Science and Technology (DST), Government of India. S.G. acknowledges support from the Science and Engineering Research Board, Department of Science and Technology, Government of India, through Project No. CRG/2021/002597.

## APPENDIX: BOGOLIUBOV-DE GENNES ANALYSIS

The fluctuation  $\delta\Psi(r, t)$  to the equilibrium order parameter in Eq. (9) is  $\delta\Psi(r, t) = u(r)e^{-i\omega t} - v^*(r)e^{i\omega t}$ , where  $u(r)$  and  $v(r)$  are Bogoliubov amplitudes and  $\omega$  is the excitation frequency. Linearization of the three coupled Gross-Pitaevskii Eqs. (3a) and (3b) and the conjugate set of equations using perturbed order parameter in Eq. (9) yields the following six coupled BdG equations:

$$\begin{aligned} \omega u_{+1} = & \left[ -\frac{\nabla_r^2}{2} + \frac{r^2}{2} + \delta + \frac{(l_q + l_z + 1)^2}{2} - \mu + c_0(2R_{+1}^2 + R_0^2 + R_{-1}^2) + c_1(2R_{+1}^2 + R_0^2 - R_{-1}^2) \right] u_{+1} \\ & + \left[ \frac{\Omega(r)}{\sqrt{2}} + R_{+1}R_0(c_0 + c_1) + 2c_1R_0R_{-1} \right] u_0 + R_{+1}^2(c_0 + c_1)v_{+1} + R_{+1}R_0(c_0 + c_1)v_0 \\ & + R_{+1}R_{-1}(c_0 - c_1)u_{-1} + (R_{+1}R_{-1}(c_0 - c_1) + 2c_1R_0^2)v_{-1}, \end{aligned} \quad (\text{A1a})$$

$$\begin{aligned} -\omega v_{+1} = & \left[ -\frac{\nabla_r^2}{2} + \frac{r^2}{2} + \delta + \frac{(l_q + l_z + 1)^2}{2} - \mu + c_0(2R_{+1}^2 + R_0^2 + R_{-1}^2) - c_1(2R_{+1}^2 + R_0^2 - R_{-1}^2) \right] v_{+1} \\ & + \left[ \frac{\Omega(r)}{\sqrt{2}} + R_{+1}R_0(c_0 + c_1) + 2c_1R_0R_{-1} \right] v_0 + R_{+1}^2(c_0 + c_1)u_{+1} + R_{+1}R_0(c_0 + c_1)u_0 \\ & + R_{+1}R_{-1}(c_0 - c_1)v_{-1} + [R_{+1}R_{-1}(c_0 - c_1) + 2c_1R_0^2]u_{-1}, \end{aligned} \quad (\text{A1b})$$

$$\begin{aligned} \omega u_0 = & \left[ -\frac{\nabla_r^2}{2} + \frac{r^2}{2} + \frac{(l_q + l_z)^2}{2} - \mu + c_0(R_{+1}^2 + 2R_0^2 + R_{-1}^2) - c_1(R_{+1}^2 + R_{-1}^2) \right] u_0 + \left[ \frac{\Omega(r)}{\sqrt{2}} - R_{+1}^2(c_0 + c_1) \right] u_{+1} \\ & + R_{+1}R_0(c_0 + c_1)v_{+1} + (c_0R_0^2 + 2c_1R_{+1}R_{-1})v_0 + \left[ \frac{\Omega(r)}{\sqrt{2}} + R_0R_{-1}(c_0 + c_1) - 2c_2R_{+1}R_0 \right] u_{-1} \\ & + R_{+1}R_{-1}(c_0 + c_1)v_{-1} \end{aligned} \quad (\text{A1c})$$

$$\begin{aligned} -\omega v_0 = & \left[ -\frac{\nabla_r^2}{2} + \frac{r^2}{2} + \frac{(l_q + l_z)^2}{2} - \mu + c_0(R_{+1}^2 + 2R_0^2 + R_{-1}^2) - c_1(R_{+1}^2 + R_{-1}^2) \right] v_0 + \left[ \frac{\Omega(r)}{\sqrt{2}} - R_{+1}^2(c_0 + c_1) \right] v_{+1} \\ & + R_{+1}R_0(c_0 + c_1)u_{+1} + (c_0R_0^2 + 2c_1R_{+1}R_{-1})u_0 + \left[ \frac{\Omega(r)}{\sqrt{2}} + R_0R_{-1}(c_0 + c_1) - 2c_1R_{+1}R_0 \right] v_{-1} \\ & + R_{+1}R_{-1}(c_0 + c_1)u_{-1} \end{aligned} \quad (\text{A1d})$$

$$\begin{aligned} \omega u_{-1} = & \left[ -\frac{\nabla_r^2}{2} + \frac{r^2}{2} - \delta + \frac{(l_q + l_z - 1)^2}{2} - \mu + c_0(R_{+1}^2 + R_0^2 + 2R_{-1}^2) + c_1(2R_{-1}^2 + R_0^2 - R_{+1}^2) \right] u_{-1} \\ & + \left[ \frac{\Omega(r)}{\sqrt{2}} + R_0R_{-1}(c_0 + c_1) + 2c_1R_{+1}R_0 \right] u_0 + (c_0 - c_1)R_{+1}R_{-1}u_{+1} \\ & + (R_{+1}R_{-1}(c_0 - c_1) + 2c_1R_0^2)v_{+1} + R_{-1}^2(c_0 + c_1)v_{-1} + R_{+1}R_0(c_0 + c_1)v_0 \end{aligned} \quad (\text{A1e})$$

$$\begin{aligned} -\omega v_{-1} = & \left[ -\frac{\nabla_r^2}{2} + \frac{r^2}{2} - \delta + \frac{(l_q + l_z - 1)^2}{2} - \mu + c_0(R_{+1}^2 + R_0^2 + 2R_{-1}^2) + c_1(2R_{-1}^2 + R_0^2 - R_{+1}^2) \right] v_{-1} \\ & + \left[ \frac{\Omega(r)}{\sqrt{2}} + R_0R_{-1}(c_0 + c_1) + 2c_1R_{+1}R_0 \right] v_0 + (c_0 - c_1)R_{+1}R_{-1}v_{+1} \\ & + (R_{+1}R_{-1}(c_0 - c_1) + 2c_1R_0^2)u_{+1} + R_{-1}^2(c_0 + c_1)u_{-1} + R_{+1}R_0(c_0 + c_1)u_0, \end{aligned} \quad (\text{A1f})$$

where  $\nabla_r^2 = -\partial^2/(2\partial r^2) - \partial/(2r\partial r)$ , and  $l_z = 1$  for phase I and 0 for phase II. To solve coupled Eqs. (A1a)–(A1f), we use the finite-difference method to discretize these equations over the spatial radial grid [43], thus transforming the BdG equations to a matrix eigenvalue equation, which can be solved using standard matrix diagonalization subroutines. To discretize the BdG equations, we used a radial grid consisting of  $N_r = 256$  points with a radial step size of  $\Delta r = 0.05$ , which results in a  $6N_r \times 6N_r$  matrix eigenvalue problem. It is noted that Eqs. (A1a)–(A1f), for  $l_z = 0$  and  $\delta = 0$ , remain invariant if  $l_q \neq 0$  is changed to  $-l_q$  with simultaneous interchange of the  $j = +1$  and  $j = -1$  components. It implies that for a nonzero magnetic quantum number of excitation ( $l_q \neq 0$ ),  $\pm l_q$  excitation modes in the single-particle excitation spectrum, viz. Fig. 5, will be degenerate. For the same reason,  $\pm l_q$  modes with  $l_q \neq 0$  of a polar-core vortex solution are also degenerate, for example, in Fig. 6(c). In the presence of detuning ( $\delta \neq 0$ ) or angular momentum ( $l_z \neq 0$ ), this invariance is not there, and as a result,  $\pm l_q$  excitations with  $l_q \neq 0$  are no longer degenerate in the coreless vortex phase.

- [1] Y.-J. Lin, K. Jiménez-García, and I. B. Spielman, *Nature (London)* **471**, 83 (2011).
- [2] D. Campbell, R. Price, A. Putra, A. Valdés-Curiel, D. Trypogeorgos, and I. Spielman, *Nat. Commun.* **7**, 10897 (2016).
- [3] X. Luo, L. Wu, J. Chen, Q. Guan, K. Gao, Z.-F. Xu, L. You, and R. Wang, *Sci. Rep.* **6**, 18983 (2016).
- [4] N. Goldman, G. Juzeliūnas, P. Öhberg, and I. B. Spielman, *Rep. Prog. Phys.* **77**, 126401 (2014).
- [5] C. Wang, C. Gao, C.-M. Jian, and H. Zhai, *Phys. Rev. Lett.* **105**, 160403 (2010).
- [6] G. I. Martone, F. V. Pepe, P. Facchi, S. Pascazio, and S. Stringari, *Phys. Rev. Lett.* **117**, 125301 (2016).
- [7] B. Ramachandhran, B. Opanchuk, X.-J. Liu, H. Pu, P. D. Drummond, and H. Hu, *Phys. Rev. A* **85**, 023606 (2012).
- [8] E. Ruokokoski, J. A. M. Huhtamäki, and M. Möttönen, *Phys. Rev. A* **86**, 051607(R) (2012).
- [9] C. J. Pethick and H. Smith, *Bose-Einstein Condensation in Dilute Gases* (Cambridge University Press, Cambridge, 2008).
- [10] L. Pitaevskii and S. Stringari, *Bose-Einstein Condensation and Superfluidity* (Oxford University Press, New York, 2016), Vol. 164.
- [11] M. A. Khamehchi, Y. Zhang, C. Hamner, T. Busch, and P. Engels, *Phys. Rev. A* **90**, 063624 (2014).
- [12] S.-C. Ji, L. Zhang, X.-T. Xu, Z. Wu, Y. Deng, S. Chen, and J.-W. Pan, *Phys. Rev. Lett.* **114**, 105301 (2015).
- [13] L. Chen, H. Pu, Z.-Q. Yu, and Y. Zhang, *Phys. Rev. A* **95**, 033616 (2017).
- [14] K. T. Geier, G. I. Martone, P. Hauke, and S. Stringari, *Phys. Rev. Lett.* **127**, 115301 (2021).
- [15] Rajat, A. Roy, and S. Gautam, *Phys. Rev. A* **106**, 013304 (2022).
- [16] D. Zhang, T. Gao, P. Zou, L. Kong, R. Li, X. Shen, X.-L. Chen, S.-G. Peng, M. Zhan, H. Pu, and K. Jiang, *Phys. Rev. Lett.* **122**, 110402 (2019).
- [17] H.-R. Chen, K.-Y. Lin, P.-K. Chen, N.-C. Chiu, J.-B. Wang, C.-A. Chen, P. Huang, S.-K. Yip, Y. Kawaguchi, and Y.-J. Lin, *Phys. Rev. Lett.* **121**, 113204 (2018).
- [18] P.-K. Chen, L.-R. Liu, M.-J. Tsai, N.-C. Chiu, Y. Kawaguchi, S.-K. Yip, M.-S. Chang, and Y.-J. Lin, *Phys. Rev. Lett.* **121**, 250401 (2018).
- [19] Y.-X. Hu, C. Miniatura, and B. Grémaud, *Phys. Rev. A* **92**, 033615 (2015).
- [20] M. DeMarco and H. Pu, *Phys. Rev. A* **91**, 033630 (2015).
- [21] K. Sun, C. Qu, and C. Zhang, *Phys. Rev. A* **91**, 063627 (2015).
- [22] C. Qu, K. Sun, and C. Zhang, *Phys. Rev. A* **91**, 053630 (2015).
- [23] L. Chen, H. Pu, and Y. Zhang, *Phys. Rev. A* **93**, 013629 (2016).
- [24] S.-G. Peng, K. Jiang, X.-L. Chen, K.-J. Chen, P. Zou, and L. He, *AAPPS Bulletin* **32**, 36 (2022).
- [25] J. Xu and J. Li, *Mod. Phys. Lett. B* **34**, 2050241 (2020).
- [26] Y. Duan, Y. M. Bidasyuk, and A. Surzhykov, *Phys. Rev. A* **102**, 063328 (2020).
- [27] X.-L. Chen, S.-G. Peng, P. Zou, X.-J. Liu, and H. Hu, *Phys. Rev. Res.* **2**, 033152 (2020).
- [28] N. Chiu, Y. Kawaguchi, S. Yip, and Y. Lin, *New J. Phys.* **22**, 093017 (2020).
- [29] Y. M. Bidasyuk, K. S. Kovtunencko, and O. O. Prikhodko, *Phys. Rev. A* **105**, 023320 (2022).
- [30] I. Vasić and A. Balaž, *Phys. Rev. A* **94**, 033627 (2016).
- [31] K.-J. Chen, F. Wu, J. Hu, and L. He, *Phys. Rev. A* **102**, 013316 (2020).
- [32] Y. Kawaguchi and M. Ueda, *Phys. Rep.* **520**, 253 (2012).
- [33] T. Isoshima and K. Machida, *Phys. Rev. A* **66**, 023602 (2002).
- [34] A. Roy, S. Pal, S. Gautam, D. Angom, and P. Muruganandam, *Comput. Phys. Commun.* **256**, 107288 (2020).
- [35] P. Kaur, A. Roy, and S. Gautam, *Comput. Phys. Commun.* **259**, 107671 (2021).
- [36] R. Ravisankar, D. Vudragović, P. Muruganandam, A. Balaž, and S. K. Adhikari, *Comput. Phys. Commun.* **259**, 107657 (2021).
- [37] P. Banger, P. Kaur, and S. Gautam, *Int. J. Mod. Phys. C* **33**, 2250046 (2022).
- [38] P. Banger, P. Kaur, A. Roy, and S. Gautam, *Comput. Phys. Commun.* **279**, 108442 (2022).
- [39] E. G. M. van Kempen, S. J. J. M. F. Kokkelmans, D. J. Heinzen, and B. J. Verhaar, *Phys. Rev. Lett.* **88**, 093201 (2002).
- [40] M. Theis, G. Thalhammer, K. Winkler, M. Hellwig, G. Ruff, R. Grimm, and J. H. Denschlag, *Phys. Rev. Lett.* **93**, 123001 (2004).
- [41] V. M. Pérez-García, H. Michinel, J. I. Cirac, M. Lewenstein, and P. Zoller, *Phys. Rev. Lett.* **77**, 5320 (1996).
- [42] A. L. Gaunt, T. F. Schmidutz, I. Gotlibovych, R. P. Smith, and Z. Hadzibabic, *Phys. Rev. Lett.* **110**, 200406 (2013).
- [43] Y. Gao and Y. Cai, *J. Comput. Phys.* **403**, 109058 (2020).